Received: 20 January 2022 | Revised: 5 August 2022 | Accepted: 8 August 2022

DOI: 10.1002/mp.15942

RESEARCH ARTICLE

MEDICAL PHYSICS

Spectral calibration of photon-counting detectors at high photon flux

Emil Y. Sidky[1] | **Emily R. Paul**[1] | **Taly Gilat-Schmidt**[2] | **Xiaochuan Pan**[1]

[1]Department of Radiology, The University of Chicago, Chicago, Illinois, USA

[2]Department of Biomedical Engineering, Marquette University and Medical College of Wisconsin, Milwaukee, Wisconsin, USA

Correspondence
Emil Y. Sidky, Department of Radiology, The University of Chicago, 5841 S. Maryland Ave., Chicago, IL 60637, USA.
Email: sidky@uchicago.edu

Funding information
National Institutes of Health, Grant/Award Numbers: R01-EB023968, R01-EB026282, R21-CA263660

Abstract

Background: Calibration of photon-counting detectors (PCDs) is necessary for quantitatively accurate spectral computed tomography (CT), but the calibration process can be complicated by nonlinear flux-dependent physical factors such as pulse pile-up.

Purpose: This work develops a method for spectral sensitivity calibration of a PCD-based spectral CT system that incorporates nonlinear flux dependence and can thus be employed at high photon flux.

Methods: A calibration model for the spectral response and polynomial flux dependence is proposed, which incorporates prior x-ray source spectrum and PCD models and that has a small set of parameters for adjusting to the spectral CT system of interest. The model parameters are determined by fitting transmission data from a known object of known composition: a step-wedge phantom composed of different thicknesses of aluminum, a bone equivalent, and polymethyl methacrylate (PMMA), a soft-tissue equivalent. This fitting employs Tikhonov regularization, and the regularization strength and the polynomial order for the intensity modeling are determined by bias and variance analysis. The spectral calibration and nonlinear intensity correction is validated on transmission measurements through a third material, Teflon, at different x-ray photon flux levels.

Results: The nonlinear intensity dependence is determined to be accurately accounted for with a third-order polynomial. The calibrated spectral CT model accurately predicts Teflon transmission to within 1% for flux levels up to 50% of the detector maximum.

Conclusions: The proposed PCD calibration method enables accurate physical modeling necessary for quantitative imaging in spectral CT. Furthermore, the model applies to high flux settings so that acquisition times will not be limited by restricting the spectral CT system to low flux levels.

KEYWORDS
calibration, photon-counting detectors, spectrum estimation

1 | INTRODUCTION

Quantitative computed tomography (CT) imaging for medical subjects can be accomplished with dual-energy scanning, because the subject can be decomposed fairly accurately into two basis materials such as bone and water. When three materials are present, dual-energy can still provide quantitative virtual monochromatic CT images,[1] but quantitative material decomposition is only possible with additional constraints in the dual-energy data processing.[2] Photon-counting detectors (PCDs) have been actively investigated for application in spectral CT, because they have the ability to simultaneously acquire x-ray transmission data with multiple x-ray spectral sensitivities. Photon-counting-based spectral CT can enable direct quantitative imaging of subjects composed of more than two types of tissues/materials.[3] In medical

imaging, a material expansion into three or more basis materials can arise in imaging patients with metal[4] or when using K-edge contrast agents.[5] In addition to enabling decomposition of more materials, PCDs have additional potential advantages for quantitative material decomposition, such as improved spatial resolution and improved dose efficiency.[6,7]

Quantitative imaging relies on accurate data modeling for the transmitted photon counts. Accordingly, it is important to calibrate the spectral response of the system, which includes the x-ray source spectrum and PCD spectral response. This system response can be estimated from x-ray transmission measurements through a known object.[8–12] Additional physics of the PCD photon detection can alter the spectral response[13] and impact the relationship between transmitted and detected photon fluence. In particular, pulse pile-up can cause this relationship to be nonlinear; for example, see Figure 13 of Danielsson et al.[14] The nonlinearity in the photon flux can compromise the spectrum estimation technique, which assumes that the detected photon flux is linearly related to the transmitted photon flux. In this work, we extend our previous spectrum estimation technique to include modeling of the nonlinear relationship between transmitted and detected photon fluence that accounts for the bulk of the PCD flux-dependence. Dickmann et al.[15] presented one method for extending spectrum calibration from transmission measurements by allowing for a spectral sensitivity function that depends on the photon flux of the incident x-ray beam. The approach we pursue here is to augment the x-ray transmission model, which includes a flux-independent spectral response, with a polynomial function that relates the transmitted and detected x-ray photon fluence. The coefficients of this polynomial along with spectral response parameters are estimated from transmission measurements through a step-wedge phantom containing discrete, known thicknesses of aluminum and polymethyl methacrylate (PMMA).

The paper is organized as follows. In Section 2, the x-ray transmission model with nonlinear photon fluence detection efficiency is presented; the spectrum/fluence-response (SFR) estimation method is outlined; and a variability analysis using noise realizations is devised that allows for hyper-parameters of the SFR estimation to be determined. In Section 3, SFR estimation is applied to experimental data for PCD calibration at different x-ray source photon flux levels. The impact and determination of the hyper-parameter settings for SFR estimation is shown. Experimental validation of SFR estimation is performed by the prediction of x-ray transmission through a Teflon slab at different photon flux levels. Results are also shown for inversion of the calibrated model, yielding Teflon slab thickness from x-ray transmission measurements.

2 | METHODS

2.1 | Spectrum estimation model

To develop the SFR model, we start with the expression for the transmission of x-ray photons given the spectral response of the PCD-based x-ray system

$$N_{w\ell} = \int S_w(E) \exp\left[-\int_\ell \mu(E,\vec{r}(x))dx\right] dE, \quad (1)$$

where $N_{w\ell}$ is the mean transmitted x-ray photon fluence along ray ℓ in PCD energy window w; x is a parameter indicating location along ℓ; $S_w(E)$ is the spectral response, noting that this function is the product of the x-ray source spectral distribution of emitted photons and the detector response for energy window w; and $\mu(E,\vec{r}(x))$ is the energy and spatially dependent linear x-ray attenuation coefficient. The goal of spectrum estimation is to determine the functions $S_w(E)$ from measurements of $N_{w,\ell}$ and a known linear x-ray attenuation coefficient map $\mu(E,\vec{r})$. In the experimental set-up, a step-wedge phantom is constructed that contains $N_m = 2$ known materials with known discrete thicknesses $t_{m\ell}$.

Discretizing and normalizing the energy integral yields the discretized transmission model

$$T_{w\ell} = N_{w\ell}/N_{0,w} = \sum_i s_{wi} \exp\left[-\sum_m^{N_m} \mu_{mi} t_{m\ell}\right] \Delta E, \quad (2)$$

where $T_{w\ell}$ is the mean fluence transmission fraction; $N_{0,w}$ is the x-ray air fluence transmission for energy window w; s_{wi} is the normalized spectral response discretized over the energy index i

$$s_w(E) = \frac{S_w(E)}{\int S_w(E)dE}$$
$$s_{wi} = s_w(E_i); \quad (3)$$

ray index ℓ now indicates discrete thickness combinations of the materials in the step-wedge phantom indexed by m; μ_{mi} is the energy discretized linear attenuation coefficient $\mu_m(E)$, which is tabulated from Hubbell and Seltzer[16]; the material thicknesses $t_{m\ell}$ represent the pathlength of material m in the calibration phantom along ray ℓ; and ΔE is the energy discretization width.

If the PCD were able to register the exact photon count number that passed through the calibration object, Equation (2) could be used directly to determine the normalized spectral response, s_{wi}, using the known pathlength values $t_{m\ell}$ of the step-wedge phantom and the measured transmission fractions $T_{w\ell}$. Once the

normalized spectral response is known, this same equation can be used for spectral CT modeling, where the values t_m become the unknown basis material sinograms. We note that the basis materials used for the spectral CT data model do not have to be the same as the basis materials used for the calibration process. For image reconstruction, the model in Equation (2) is either inverted directly, obtaining t_m as a function of T_w, or implicitly, where this model is part of a complete data model relating the basis material spatial distribution with the transmitted x-ray fraction.

If the PCD does not register the same photon count number that passed through the scanned object, which can happen due to flux-dependent effects such as pulse pile-up, use of the model in Equation (2) for spectral CT can lead to artifacts in the resulting images. One solution is to run the CT acquisition at low x-ray flux levels so that nonlinearity in the detector response is minimal, and we have done so successfully in, for example, Schmidt et al.[17] In this work, we seek to augment the transmission data model to account for the nonlinear flux-dependent effects so that the spectral CT acquisition can be performed at higher x-ray source flux levels.

2.2 | Spectrum/fluence-response estimation model

For the SFR model, parameters are introduced to account for the nonlinear relationship between transmitted photon fluence and the detected photon fluence in addition to the unknown spectra s_{wi}. The unknown spectral response can be modeled directly using early stopping, as done in Sidky et al.,[8] or explicit regularization to address the ill-conditionedness of the spectrum estimation problem. Because we are including additional undetermined parameters for the nonlinear response modeling, we employ a low-dimensional spectrum representation developed in Perkhounkov et al.[18] so as to decrease the reliance on explicit regularization for obtaining stable solutions.

2.2.1 | Spectral response modeling

We seek to represent the spectra with a low-dimensional parameterization taking advantage of prior estimates on the x-ray source spectrum and PCD spectral response. The continuous, unnormalized spectral sensitivity is expressed as

$$S_w(E,\beta) = D_w(E)R(E)\exp\left(-\sum_{j=1}^{N_\beta}\beta_{w,j}(E/E_{\max})^j\right), \quad (4)$$

where $D_w(E)$ is the detector response model for window w; $R(E)$ is the x-ray source spectrum model; and the exponential factor with a polynomial function allows for overall modification of the spectral response as needed to fit the transmission measurements; that is, coefficients β_j are unknown a priori. Even if a prior model of the detector response and source spectrum is known, the polynomial correction is still needed to adjust for detector element variation. The particular functional form of the correction as an exponential of a polynomial is used because it cannot be negative; choosing the polynomial order N_β to be an even number results in a decaying function in both directions of energy E for positive $\beta_{i=N_\beta}$.[18] The corresponding discrete, normalized spectral response, $s_{wi}(\beta)$, is obtained by substituting Equation (4) into Equation (2)

$$s_w(E,\beta) = \frac{S_w(E,\beta)}{\int S_w(E,\beta)dE} \quad (5)$$

$$s_{wi}(\beta) = s_w(E_i,\beta).$$

2.2.2 | Nonlinear fluence modeling

When modeling PCDs, the detection physics are known to cause a flux-dependent distortion of the PCD spectral response[19,20] or inter-pixel dependences if operated in the charge-summing mode. Here, we consider the pixels to be independent of each other and we consider a simplified nonlinear response, where the distribution of the spectral response of a given energy window does not change with flux; rather, we only allow for the measured photon flux for energy window w to deviate from the modeled, post-object flux for w. Mathematically, the measured flux for window w and ray ℓ is

$$I_{w\ell}^{\text{meas}} = N_{w\ell}^{\text{meas}}/t = f(N_{w\ell}/t), \quad (6)$$

where t is the acquisition time; $N_{w\ell}^{\text{meas}}$ is the photon count registered by the PCD; $N_{w\ell}$ is the model fluence as given by Equation (1); and $f(\cdot)$ is a nonlinear smooth function that relates the two. Ideally, $f(\cdot)$ would be the identity function, but due to effects such as pulse pile-up $f(\cdot)$ deviates from the identity function. Because it is more convenient to work with fractional fluence instead of flux, we consider a nonlinear relationship between the modeled transmitted fluence fraction post-object $T_{w\ell}^{\text{trans}}$ and the measured transmitted fluence fraction $T_{w\ell}^{\text{meas}}$. In the Appendix, we explain the connection between the flux-dependent relationship and the fractional fluence-dependent relationship. Interestingly, the N-dependent relationship does not depend on the acquisition time. In the following, we use the superscripts "data", "meas", and "trans" to refer, respectively, to the actual PCD data, our

model of the PCD data, and the data model post-object.

We assume that the transmission fractional fluence incident to the PCD can be related to the measured transmission fractional fluence by a low-order polynomial expression. Substituting the spectrum model from Equation (5) into the fluence model Equation (2) yields the transmission fractional fluence model

$$T^{\text{trans}}_{w\ell}(\beta) = \sum_i s_{wi}(\beta) \exp\left[-\sum_m \mu_{mi} t_{m\ell}\right] \Delta E. \quad (7)$$

The models for the measured and transmission fractional fluences are then related by the polynomial

$$F_w(T, \alpha) = T + \sum_{k=0}^{N_\alpha} \alpha_{w,k} T^k \quad (8)$$

$$T^{\text{meas}}_{w\ell}(\alpha, \beta) = F_w(T^{\text{trans}}_{w\ell}(\beta), \alpha). \quad (9)$$

This polynomial expression is formulated so that $T^{\text{meas}} = T^{\text{trans}}$ if all coefficients $\alpha_{w,k}$ are zero. We note here that our model relates fractional fluences, but physically the nonlinearity depends principally on the transmitted photon flux. The nonlinear relation in Equation (8) between fractional fluences is more convenient experimentally because the PCD registers photon counts and because it is the fractional fluence $T^{\text{trans}}_{w\ell}$ that is needed for sinogram estimation for image reconstruction. The justification and conditions for use of Equation (8) are presented in the Appendix.

In the low fluence limit, T^{meas} should go to zero when T^{trans} goes to zero. This physical constraint is obeyed when

$$\alpha_{w,0} = 0. \quad (10)$$

Similarly, at the other extreme, the modeled and measurement model transmission fractions should both equal to one for an air scan, and this physical constraint is obeyed when

$$\sum_k \alpha_{w,k} = 0. \quad (11)$$

Both of these relationships can either be used as constraints on the α parameters or these parameters can be left unconstrained in the optimization process and Equations (10) and (11) can be used as checks on the model validity. In this work, we take the latter approach.

We reiterate that the proposed fluence relationship in Equation (9) is written in terms of the fraction of transmitted photons because we only have access to $N^{\text{meas}}_{0,w}$, the number of photons detected in energy window w for an air scan. Without a separate measurement, we do not have access to $N^{\text{trans}}_{0,w}$. This limitation of the SFR model does not impact image reconstruction from PCD-based spectral CT because only data in the form of T^{trans} are needed.

2.3 | Spectrum/fluence-response estimation algorithm

The parameters α and β of the SFR model are found by fitting Equation (9) to a set of measured transmission data of a known object using a PCD-based x-ray system, where the x-ray source current is held fixed. Because inconsistency present in the measured data is expected to be dominated by noise due to finite quanta, the data fidelity term used for the fitting is the transmission Poisson likelihood (TPL) model. Equivalently, we use the Kullback–Leibler (KL) divergence between the measurement model $T^{\text{meas}}_{w\ell}(\alpha, \beta)$ and the actual measured transmission fractions, $T^{\text{data}}_{w\ell}$

$$\alpha^*_w, \beta^*_w = \arg\min_{\alpha,\beta} \left\{ \sum_\ell D_{\text{KL}}\left(T^{\text{data}}_{w\ell}, \max(T^{\text{meas}}_{w\ell}(\alpha, \beta), \varepsilon)\right) + \frac{\gamma}{2}\|\beta\|_2^2 \right\}, \quad (12)$$

where

$$D_{\text{KL}}(a, b) = b - a - a\log(b/a). \quad (13)$$

The thresholding of the model to values greater than ϵ is necessary to avoid computing logarithms of negative numbers, as the transmission model may become negative depending on the value of the coefficients α_k. For this work, we choose $\epsilon = 10^{-5}$. The Tikhonov regularization with parameter γ is needed to stabilize the recovery of the parameters β. Such regularization for α is not needed because we consider only low-order polynomials, $N_\alpha \leq 4$.

For the sake of clarity, we gather the equations needed to express the measurement model

$$\begin{aligned} T^{\text{meas}}_{w\ell}(\alpha, \beta) &= T^{\text{trans}}_{w\ell}(\beta) + \sum_{k=0}^{N_\alpha} \alpha_{w,k} (T^{\text{trans}}_{w\ell}(\beta))^k, \\ T^{\text{trans}}_{w\ell}(\beta) &= \sum_i s_{wi}(\beta) \exp\left[-\sum_m \mu_{mi} t_{m\ell}\right] \Delta E, \\ s_{wi}(\beta) &= S_w(E_i, \beta) / \sum_i S_w(E_i, \beta) \Delta E, \\ S_w(E, \beta) &= D_w(E) R(E) \exp\left(-\sum_{j=1}^{N_\beta} \beta_{w,j} (E/E_{\max})^j\right), \end{aligned} \quad (14)$$

where $t_{m\ell}$ are the known calibration phantom material m thicknesses along ray ℓ; E_i are the x-ray photon energies separated by constant spacing ΔE; $D_w(E)$ is a prior model for the PCD spectral response for window w if it is available, otherwise $D_w(E)$ is set to one; and $R(E)$ is a prior model for the x-ray source spectrum if it is available, otherwise $R(E)$ is set to one.

The optimization problem in Equation (12) is non-convex and because of this, the parameter initialization is critical. The transmission model is designed so that setting $\alpha = 0$ and $\beta = 0$ should provide a reasonable initial estimate. Because Equation (12) is a small-scale optimization, it is amenable to standard optimization functions available in many computational resource libraries. We selected the Broyden Fletcher Goldfarb Shanno (BFGS) algorithm as implemented in Python's scipy.optimize sub-package. BFGS is a quasi-Newton method which is explained in, for example, Nocedal and Wright.[21]

2.4 | Model inversion for spectral computed tomography image reconstruction

Because the intended application of the proposed calibration model is for spectral CT image reconstruction, we briefly outline how to use it for this purpose. For subjects with more than one basis material, Equation (14) is inverted obtaining $T^{\text{trans}}_{w,\ell}$ as a function of $T^{\text{meas}}_{w,\ell}$. This function is straightforward to invert, if the determined α coefficients result in a monotonic polynomial function over the domain [0,1]. If the flux level is too high, it is possible that this function will not be monotonic and unique inversion of Equation (14) is not possible. In such cases, where there are multiple solutions, the correct one can be identified from context. For example, a scenario where this issue might arise is in body imaging, where a high flux is needed for achieving good signal-to-noise ratio in the center of the body. Toward the periphery, the photon flux may exceed the point, where Equation (14) is monotonic. In this case, unique solution to Equation (14) can be found in the central regions of the body transmission data. If there are then multiple solutions toward the periphery, the correct solution can be identified by continuity with the central region transmission data. For the purposes of this work, we limit the flux to a level, where Equation (14) is monotonic. Once $T^{\text{trans}}_{w,\ell}$ is obtained, we have the usual model, written in Equation (2), that relates material sinograms t_m to the transmitted fluence fractions $T_{w\ell}$ and any spectral CT image reconstruction technique, for example, Schmidt et al.,[17] can be applied.

For subjects that are composed of a single basis material, the sinogram t_{smat} can be directly obtained from $T^{\text{smat-meas}}_{w,\ell}$, where we use the label "smat" to denote "single material" (or tissue). To perform this inversion, we consider the measurement model for the special case of a single material

$$\begin{aligned} T^{\text{smat-meas}}_{w\ell}(\alpha, \beta; t_{\text{smat}}) &= T^{\text{smat-trans}}_{w\ell}(\beta; t_{\text{smat}}) \\ &\quad + \sum_{k=0}^{N_\alpha} \alpha_{w,k} (T^{\text{smat-trans}}_{w\ell}(\beta; t_{\text{smat}}))^k, \\ T^{\text{smat-trans}}_{w\ell}(\beta; t_{\text{smat}}) &= \sum_i s_{wi}(\beta) \exp\left[-\mu_{\text{smat},i} t_{\text{smat}}\right] \Delta E, \end{aligned} \tag{15}$$

and the sinogram is found by solving the following equation for t_{smat} :

$$T^{\text{smat-meas}}_{w\ell}(\alpha, \beta; t_{\text{smat}}) - T^{\text{smat-data}}_{w\ell} = 0. \tag{16}$$

This can be accomplished by standard root-finding algorithms. In this work, we used Brent's method, which does not require computation of derivatives with respect to t_{smat}. Note that there are multiple energy windows w, and only one basis material; each energy window should provide different estimates of the same sinogram t_{smat}. In Section 3, this method is used to estimate the Teflon slab thickness from transmission measurements in each energy window of our PCD.

2.5 | Photon-counting detector transmission measurements

Photon-counting spectral data were acquired on a bench-top spectral CT system with a CdTe PCD (DxRay, Northridge, CA). The detector consisted of an array of 4×64, 1.4 mm $\times$ 1.0 mm pixels with four comparator channels per pixel and a dead-time of 1 μs leading to a maximum count rate of 10^6 counts/s/pixel. Data were acquired with an x-ray tube voltage of 90 kV and 2 mm aluminum filtration. The PCD detector collected data with four energy windows with thresholds of 22, 45, 55, and 65 KeV. The energy windowed data were obtained by subtracting the thresholded count measurements, and nominally counts data were obtained in the energy windows [22,45], [45,55], [55,65], and [65,90] KeV, where the fourth energy window is limited by the x-ray source potential. The model in Equation (4) incorporates an initial estimate of the x-ray spectrum, $R(E)$, and the detector spectral response for each of the four energy windows, $D_w(E)$. For $R(E)$, we use the model from Bujila et al.[22] and its accompanying software implementation is available as a Python package, SpekPy. For the PCD response $D_w(E)$, we used the model from Touch et al.[23] Plots of these functions are shown in Figure 1.

To calibrate the model, the α and β coefficients are determined by acquiring transmission data

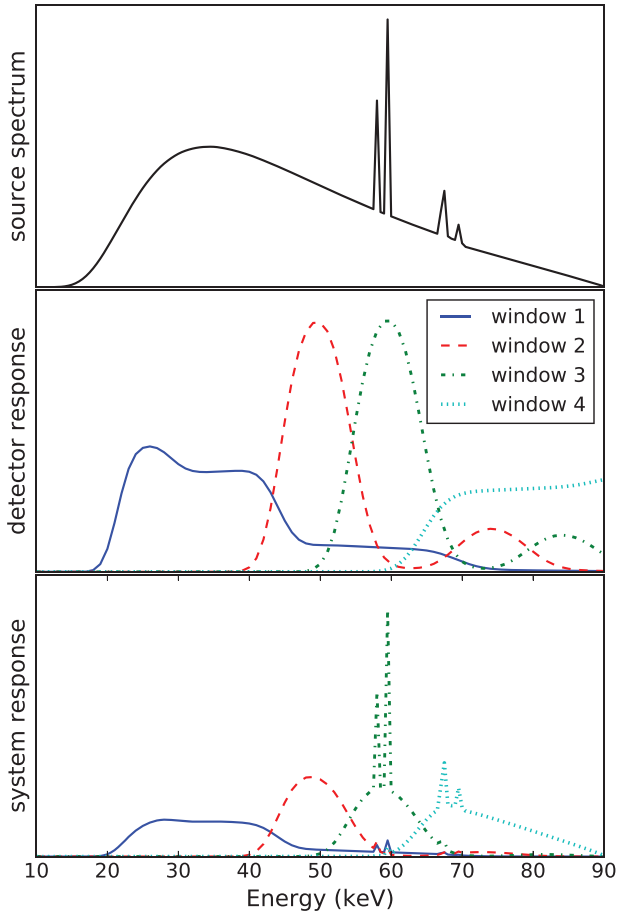

FIGURE 1 Normalized models for the x-ray source spectrum and DxRay photon-counting detector (PCD) detector response. the top and middle graphs show the functions $R(E)$ and $D_w(E)$, respectively, from Equation (4). The bottom graph shows the product $R(E)D_w(E)$

through a physical phantom of known dimension and composition. The phantom used here is a step-wedge phantom consisting of 25 combinations of PMMA and aluminum thicknesses, created by combining 0–4 PMMA slabs and 0–4 aluminum slabs. The individual PMMA and aluminum slabs have a thickness of 2.54 and 0.64 cm, respectively. A set of calibration training data was acquired at five x-ray source flux levels corresponding to 9%, 14%, 27%, 40%, and 54% of the maximum detector count rate. The acquisition time was adjusted at each flux level such that the tube current time product (total fluence) remained at constant value of 0.456 mAs across all flux settings. Solving Equation (12) using the step-wedge data yields the α and β coefficients needed to completely specify the model, Equation (4). The calibration is performed for each of the detector pixels individually. Additional transmission measurements are taken for a 3.81 cm (1.5 inch) thick slab of Teflon, at the five flux levels, in order to test the model's prediction on x-ray transmission on a different material than what comprises the calibration phantom. Because the intended application of the calibration method is for spectral CT imaging, we also used the calibrated transmission model to solve for the Teflon slab thickness based on the actual measured transmission through the Teflon slab.

2.6 | Model variability and the determination of N_α and regularization strength γ

Assessing the model variability has two purposes. Model variability can be instrumental in designing the precise setup for the SFR calibration; namely, selecting calibration phantom materials and the set of transmission pathlengths through these materials. It is also important for determining the hyper-parameters of the SFR estimation problem. The calibration setup will depend on the expected composition and size of the scanned subjects. Thus, here, we consider model variability only for the purpose of determining SFR estimation hyper-parameters. The main parameters of the transmission model in Equation (4) that are entered externally are the order of the energy polynomial, N_β, the order of the fluence polynomial N_α, and the β-regularization strength γ. Empirically, the dependence on N_β is weak, and in this work we set this parameter to

$$N_\beta = 10. \tag{17}$$

We do vary N_α and γ and explore the trade-off between fitting the calibration data and variability of the resulting calibration model.

To explore model variability, we generate simulated ideal transmission data for the step-wedge phantom from the model specified by the input parameters N_α, N_β, γ, and the solution of Equation (12), α^* and β^*. Noisy realizations are then generated using a Poisson distribution using the air scan measurements for each energy window to provide the number of incident photons for the noise model. We note that the measured air scan values will be slightly off from the true incident photon numbers, but this discrepancy does not impact the analysis. The simulated noisy transmission realizations are used as input data for Equation (12) yielding an ensemble of α and β coefficients for fixed N_α, N_β, and γ. The ensemble of both polynomial coefficients are used to generate an ensemble of x-ray spectral sensitivities, nonlinear fluence (NLF) functions, and transmission measurements through various materials/thicknesses. The relative standard deviation of these quantities characterizes the variability of the model in terms of a physical quantity of interest. For the present work, 100 noise realizations are used for the variability analysis.

3 | RESULTS

3.1 | Model fitting error

For the first set of results, PCD calibration, summarized in Equation (12), is applied to the step-wedge transmission data for all five x-ray source flux levels for different N_α and regularization strengths γ. The resulting fitting error to the transmission data is reported with the quantity

$$\Delta T_w = \sum_\ell D_{KL}\left(T_{w\ell}^{data}, T_{w\ell}^{meas}(\alpha_w^*, \beta_w^*)\right), \qquad (18)$$

where the transmission data are normalized so that the air scan has a transmission of 1.0, and the index ℓ runs through the 25 transmission measurements through the step-wedge phantom. The transmission model calibration is performed for all 64 detector pixels individually, and the reported fitting error results represent the average over all of the detector pixels.

The fitting error is displayed with the grid of plots in Figure 2. As a general trend, the fitting error increases with γ with the steepest increase occurring in the neighborhood of $\gamma = 10^{-3}$. The error does plateau at large γ, and this region corresponds to the case where the magnitude of the β coefficients becomes negligible and the spectral response of the system is $R(E)D_w(E)$.

The NLF polynomial degree does have a large impact on the fitting error. Even for the lowest flux level of 9% of the detector maximum there is a substantial improvement in going from the linear ($N_\alpha = 1$) to the quadratic ($N_\alpha = 2$) model. We note that the y-scale range is too small to see the linear case for all of the conditions, particularly at the higher flux levels. As N_α increases the fitting error decreases, but the improvement in going from $N_\alpha = 3$ to $N_\alpha = 4$ is minimal. Accordingly, we only consider cubic $N_\alpha = 3$ NLF functions.

For $N_\alpha = 3$, it is interesting that γ has little impact on the model fit for energy windows 3 and 4. The greatest impact of the regularization is seen mainly in energy window 1 and for this window, tuning γ has increasing impact as the x-ray source flux increases. That TPL dependence on γ is weak for many of the experimental window and flux measurements, indicates that the initial models for $R(E)$, the x-ray source spectrum, and for $D_w(E)$, the detector response, are reasonably accurate in reproducing the transmission measurements of the step wedge phantom. Still, the exponential-polynomial modification of the system spectral response does help to improve the fit to the calibration measurements for many of the experimental conditions thereby expanding the range of applicability of the model.

3.2 | Model fitting variability

In setting the regularization strength γ, it is important to balance the model fitting error against its variability. The variability is assessed using noise realizations of data estimated by taking as ground truth the transmission model using the fit parameters α_w^* and β_w^*. The mean standard deviation of the normalized spectrum and NLF function are shown in Figure 3 for all energy windows and flux levels, averaged over the 64 detector pixels. The variability of the spectrum is relatively high at low regularization strength and it decreases with γ. At large γ the variability in the spectrum goes to zero, because the β coefficients themselves tend to zero. The variability in the NLF function decreases more weakly with increasing γ since large α coefficients are not explicitly penalized.

Variability in the calibrated transmission model may only be an indirect measure of interest. A more direct measure of variability would be to compute variability in x-ray transmission through materials or tissues that are expected to be in the scanned subject. As an example of this, Figure 4 shows the variability for x-ray transmissions through a 1% gadolinium solution for all energy windows and flux levels as a function of regularization parameter γ. From the figure, it is clear that γ-regularization has more of an impact for the higher energy windows and that it is equally important for all flux levels. These trends are similar to the spectrum variability shown in Figure 3 except for energy window 1, where the spectrum has high variability at low γ and the gadolinium transmission does not.

3.3 | Selection of regularization strength

Selecting the regularization strength parameter γ needs to balance bias of the model against model variability. For the present demonstration of the SFR model, we note that for the cubic NLF function the increase in calibration transmission error shown in Figure 2 is a weak function of γ and we select γ based on the variability in the spectral sensitivity shown in Figure 3. In this figure, the spectral sensitivity variability is greater for energy windows 1 and 4 than it is for windows 2 and 3. Accordingly, we select the values

$$\begin{aligned}\gamma_{w=1} &= 1\times10^{-3},\\ \gamma_{w=2} &= 1\times10^{-4},\\ \gamma_{w=3} &= 1\times10^{-4},\\ \gamma_{w=4} &= 1\times10^{-3}.\end{aligned} \qquad (19)$$

With these regularization strengths and settings $N_\alpha = 3$, $N_\beta = 10$, the transmission model is completely determined.

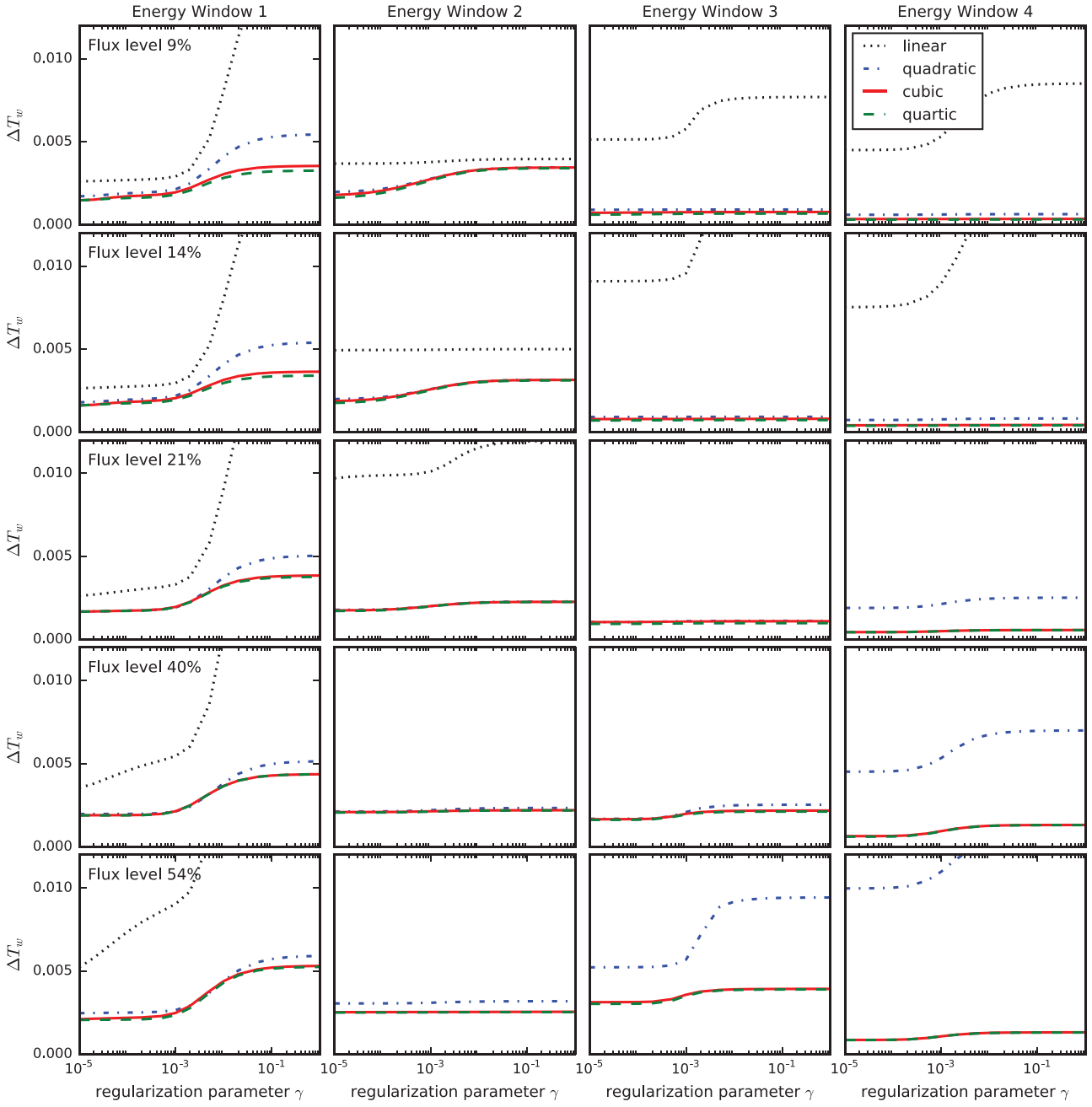

FIGURE 2 Model error as measured by ΔT_w, defined in Equation (18), averaged over all 64 detector pixels. The energy window w increases along the column index, and the x-ray flux level increases with the row index. The different curves in each panel indicate the N_α value (linear corresponds to $N_\alpha = 1$, and quartic corresponds to $N_\alpha = 4$). The x-axis of each plot indicates $\log(\gamma)$

The goodness of the fit, using these parameter settings, is indicated in the corresponding points on the graphs for the TPL calibration error results of Figure 2. Also, at these parameter settings, the checks on the α-coefficients yield a mean deviation from zero of 0.008 and 0.002 for Equations (10) and (11), respectively.

The calibrated transmission model, averaged over all 64 detector pixels, is shown in Figure 5, where both the normalized spectral sensitivity and NLF functions are shown in the left and middle columns, respectively. Interestingly, the spectral responses do not vary substantially from one x-ray source flux level to another; the change in source flux level only results in a change in the NLF functions as one might expect.

The NLF functions are mostly observed to be monotonic and therefore invertible. Notable exceptions are $w = 3$ for the 40% and 54% source flux levels, where it is seen that the solid, green curves do not increase monotonically over the full range of transmitted fractional fluence. This non-monotonic behavior complicates

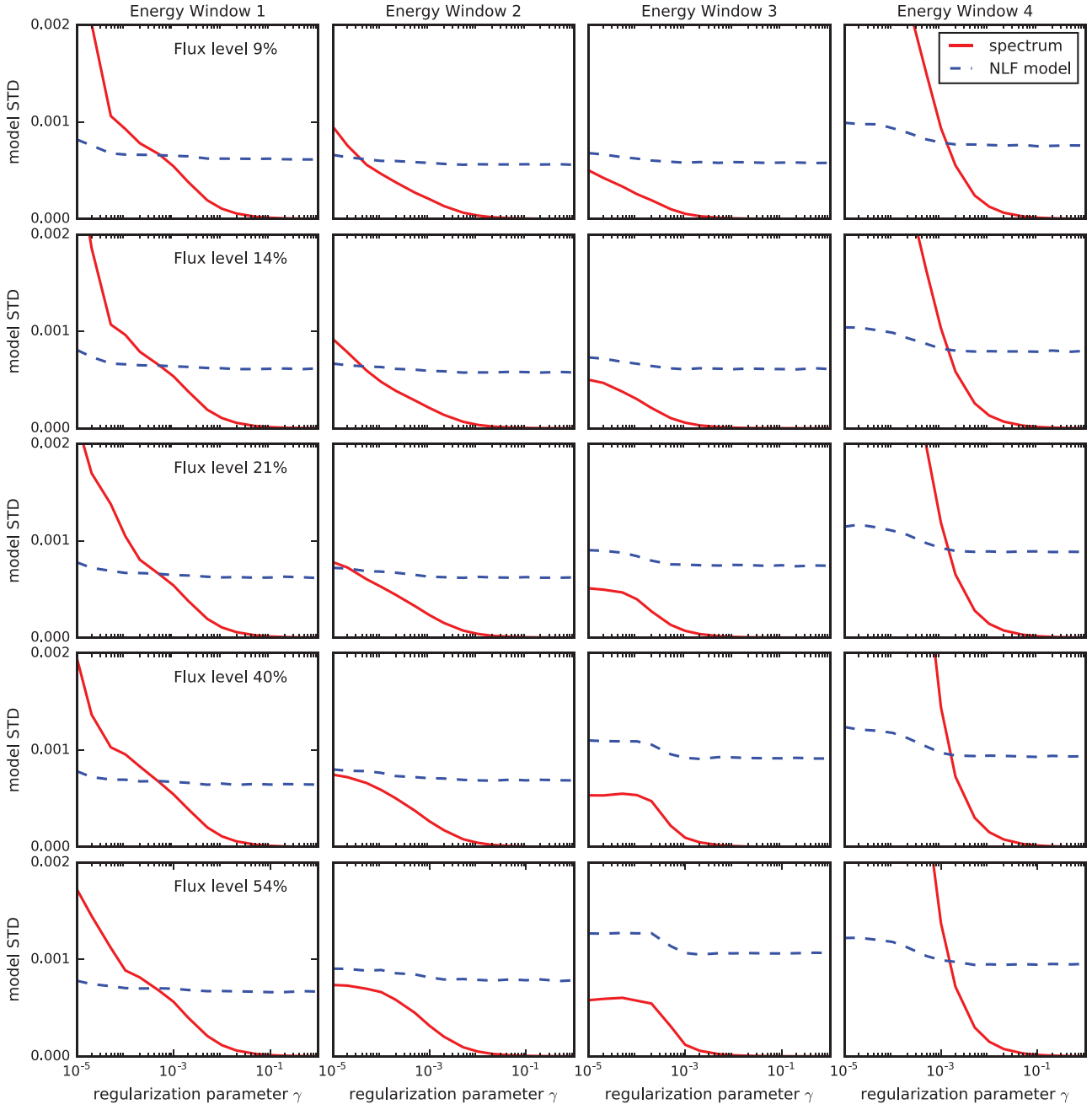

FIGURE 3 The grid of plots shows the standard deviation of the normalized spectrum model $s_w(E, \beta_w^*)$, averaged over E, and the nonlinear fluence (NLF) function $F_w(T, \alpha_w^*)$, averaged over T. Recall that the transmission fraction T varies from 0 to 1

the inversion of these NLF functions and the estimation of the transmitted fractional fluence needed for spectral CT image reconstruction, as discussed in Section 2.4. Although these curves are non-monotonic, they can still be inverted if the domain of the transmitted fractional fluence is restricted to values where the NLF is strictly increasing. This restriction does involve the assumption that the true solution is not on the branch of the function with negative slope. Thus, we do not increase the source flux level beyond 54%, as it is anticipated that the non-monotonicity would become worse.

Although we bypass the need for a function that relates fractions fluxes, it is interesting to estimate these functions from the NLF functions, and we do so without requiring a measurement of $I_{w,0}$. This can be accomplished by assuming that the nonlinear response of the PCD photon counts is due only to flux-dependent effects and that in the low flux limit the PCD registers the exact number of photons that passed through the scanned object. If this assumption holds, there is an additional boundary condition at the zero fractional flux limit; not only does the measured fractional flux go to zero in this

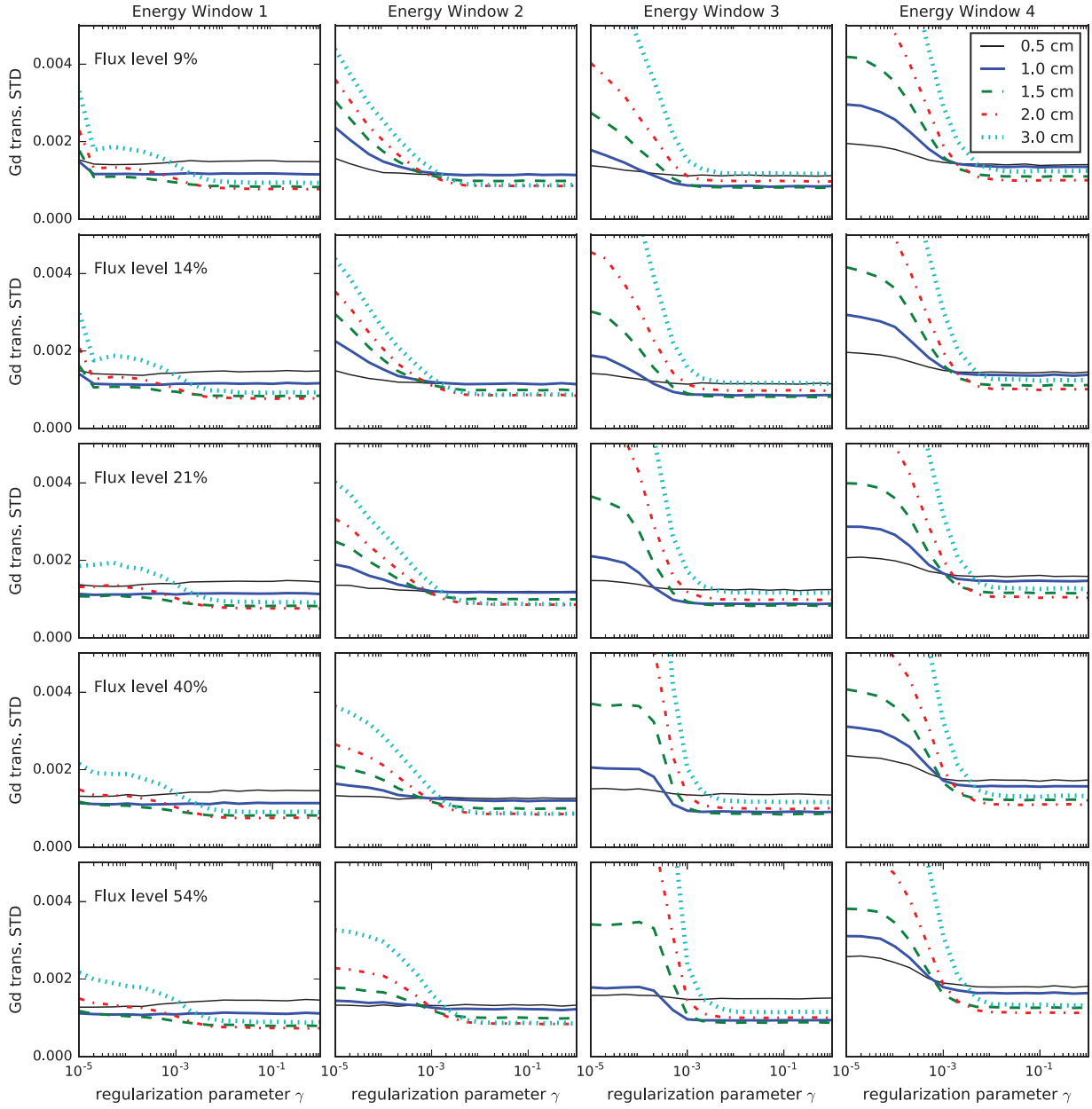

FIGURE 4 The grid of plots shows the relative standard deviation (the standard deviation divided by the mean) of x-ray transmission through a 1% gadolinium solution of different thicknesses

limit, the slope of its dependence on the post-object, transmitted, fractional flux is one. The right column of Figure 5 shows the derived non-linear fractional flux functions using this assumption.

3.4 | Model testing on Teflon transmission

3.4.1 | Teflon transmission prediction

As an independent test of the calibrated transmission model, its prediction on the transmission fraction through a Teflon block is compared with actual PCD measurements. The results for all 64 detector pixels, 4 energy windows, and 5 flux levels are shown in the top row of Figures 6–9. The comparison between the transmission model, which includes the NLF function, and the measured Teflon transmission shows good agreement for all energy windows; the largest discrepancy is seen for the low and intermediate flux levels of energy window $w = 4$ in Figure 9. Also shown are the results if the transmission model does not include the NLF function; the fit to the Teflon transmission data is markedly worse by excluding the NLF function and as expected the error is larger for higher flux levels.

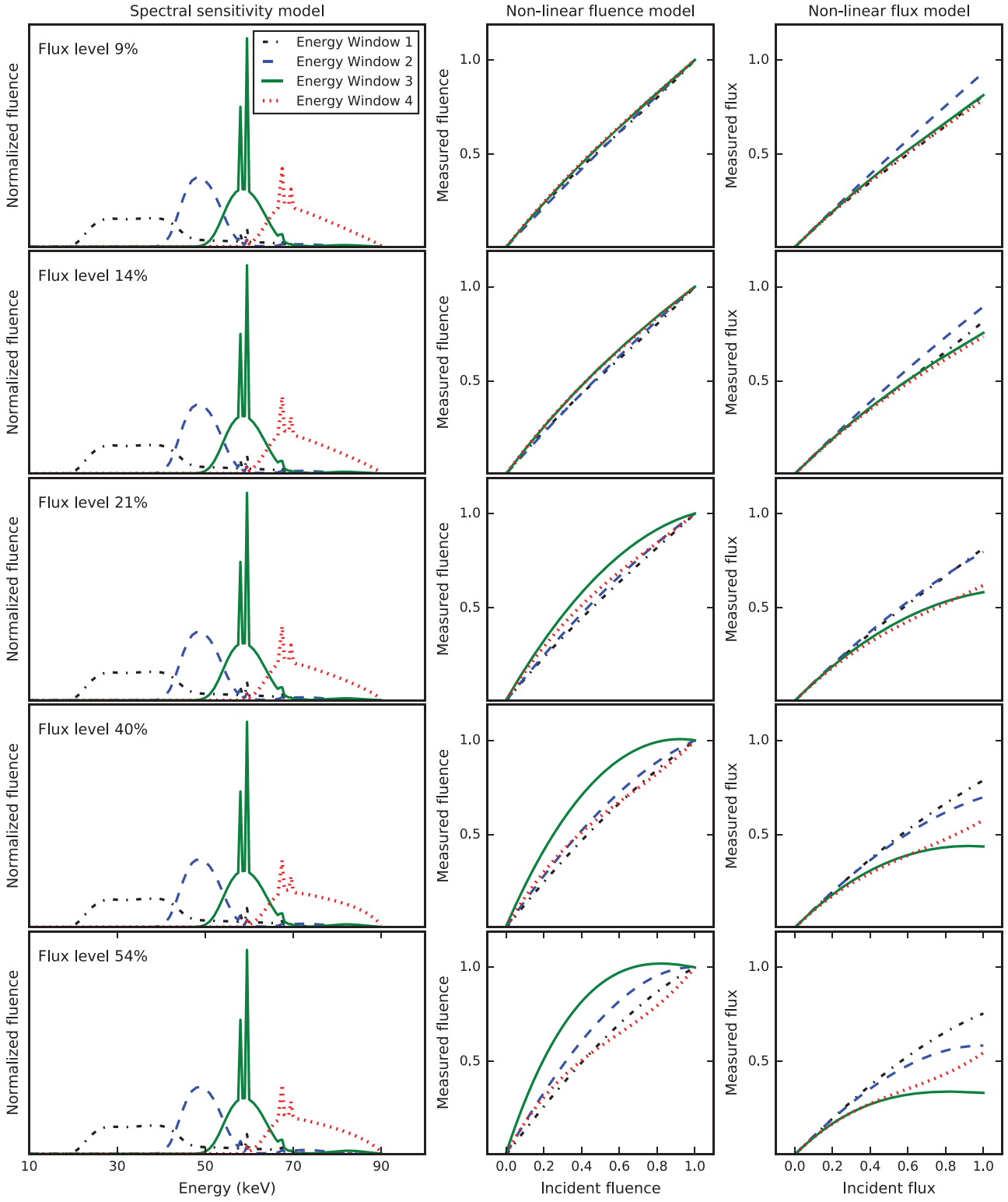

FIGURE 5 The calibrated transmission model, averaged over all 64 detector pixels, for all energy windows and different flux levels. The left column shows the normalized spectral sensitivities. The middle column shows the nonlinear fluence function, and the right column shows the nonlinear flux function based on the assumption that it is proportional to the fluence function and the slope near zero flux is unity

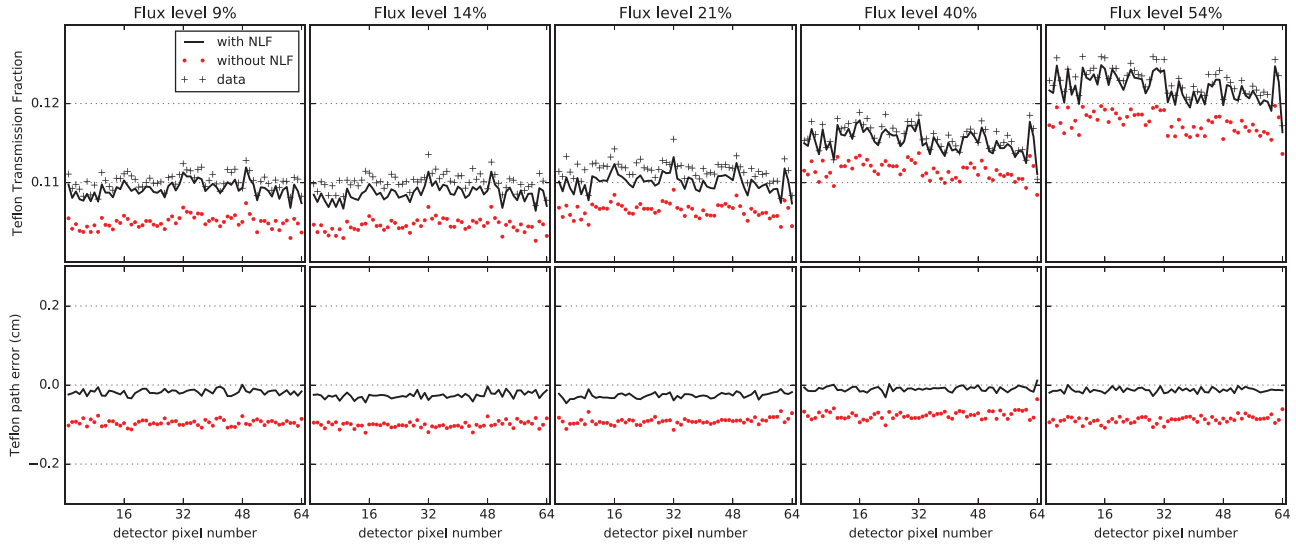

FIGURE 6 Top row: predicted x-ray transmission fractions through a 3.81 cm slab of Teflon for energy window $w = 1$ at the various flux levels. The measured transmission fraction ("+" symbols) is shown together with the calibration model without nonlinear fluence fitting (red " * " symbols) and with the proposed nonlinear fluence fitting (black curve). Bottom row: prediction of the Teflon slab thickness obtained by inverting the calibrated transmission model using the measured data as input. The Teflon slab thickness prediction is displayed as a difference from the true value of 3.81 cm

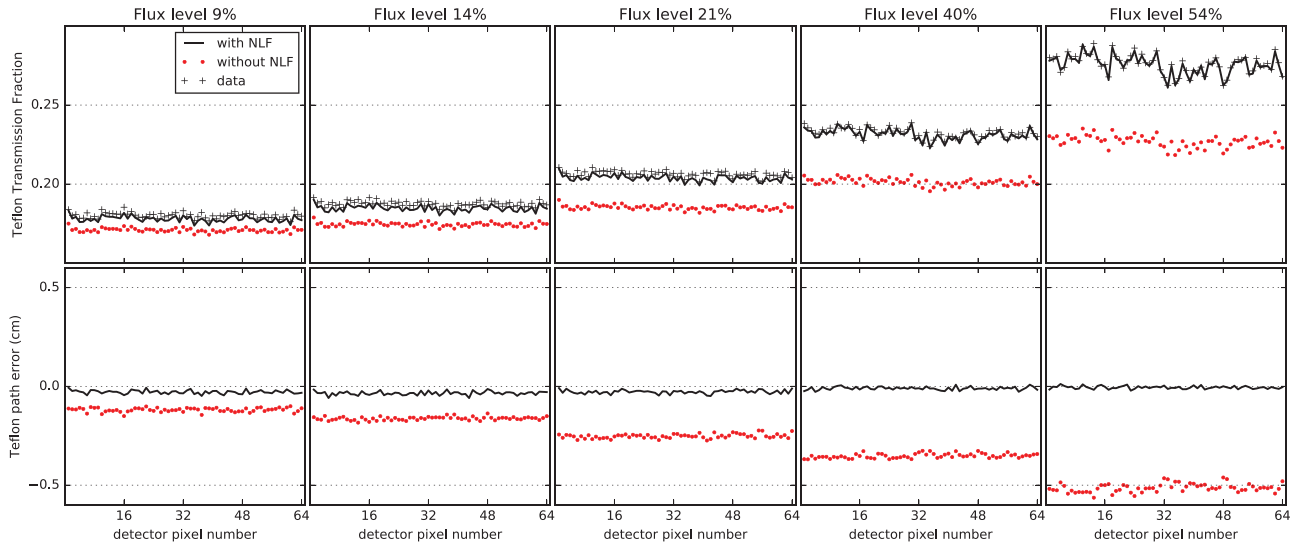

FIGURE 7 Same as Figure 6 except the displayed results are for energy window $w = 2$

There is variation in the transmission fraction over the detector pixel index; this variation is due mainly to differences in the detector pixel calibration and not noise in the measurement. This is seen in the fact that the calibrated transmission model follows all of the visible variations in the Teflon transmission measurements. To appreciate the actual error in the transmission model, we use the model to predict the Teflon slab thickness from the Teflon transmission measurements.

3.4.2 | Teflon slab thickness prediction

Because the calibration methodology presented here is developed for the purpose of spectral CT image reconstruction, a more direct test of the model for this purpose is the estimation of the Teflon slab thickness from the Teflon transmission measurements, using the methodology described in Section 2.4. The resulting prediction of the Teflon slab thickness is shown by the Teflon path

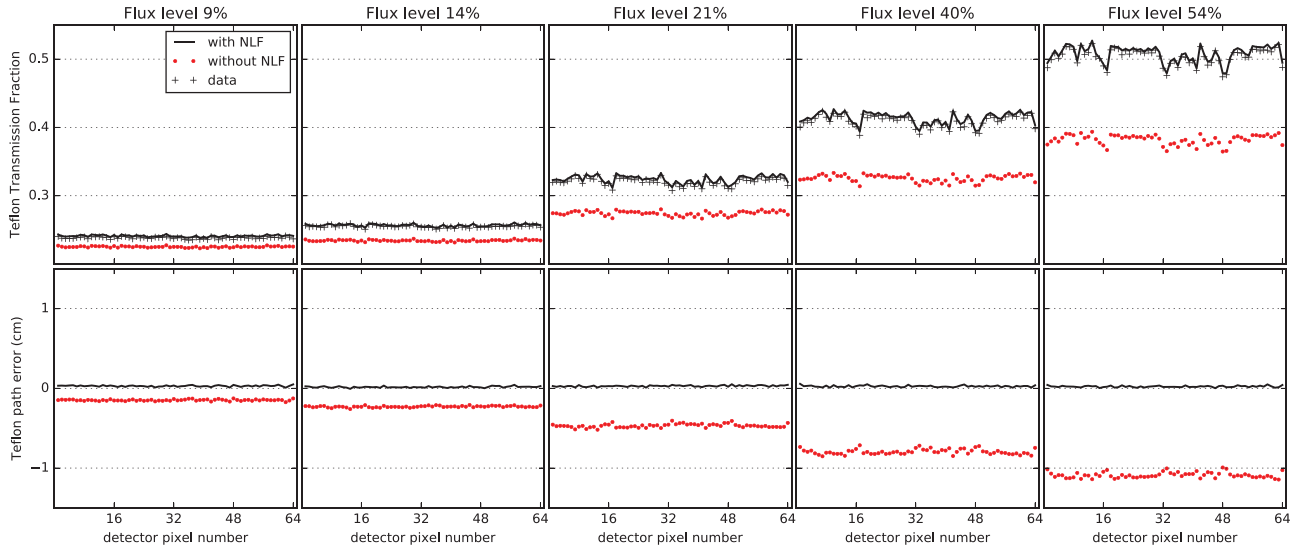

FIGURE 8 Same as Figure 6 except the displayed results are for energy window $w = 3$

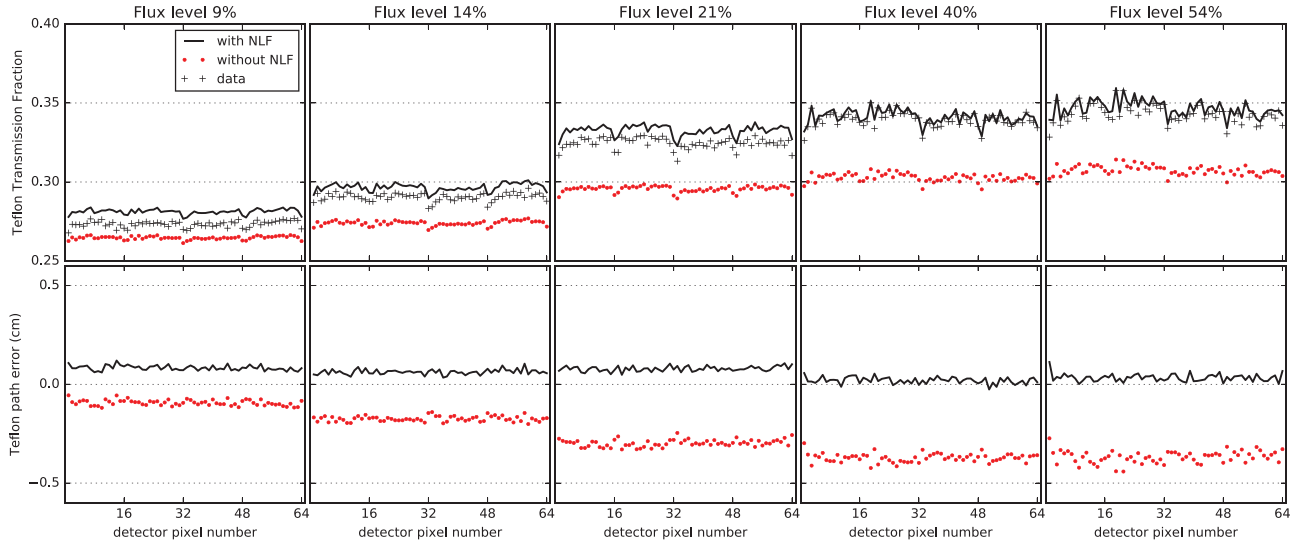

FIGURE 9 Same as Figure 6 except the displayed results are for energy window $w = 4$

error plots shown in the bottom row of Figures 6–9. The results show an agreement to a fraction of a millimeter for the use of transmission modeling with the NLF function for most of the w and x-ray source flux settings. The largest error appears for $w = 4$ at the low to intermediate flux settings. Also shown is the Teflon slab thickness prediction without the NLF function, and it is clear that this introduces substantial error. Thus, the NLF function is a critical piece of the transmission modeling.

Because the slab thickness should be uniform over all detector pixels, the variation in pixel calibration is factored out of these results and the error in the calibration process is easier to appreciate. The error in the Teflon slab thickness is seen as a deviation from zero which is caused by deterministic and statistical error in the calibration and measurement. A pixel-to-pixel variation is seen that results from noise in the Teflon measurements and, indirectly, from noise in the calibration measurements through the transmission model. There is also a systematic shift from 0 over all pixels, which is due to deterministic error that is likely introduced by the approximation that the distribution in PCD spectral response is not flux-dependent, as discussed in Section 2.2. Nevertheless the SFR model developed in this work may be useful for application to spectral CT, because the deterministic error is only slightly larger than the variations due to noise.

4 | DISCUSSION AND CONCLUSION

In applying the SFR model, it is important to identify the materials and transmission lengths of interest. This will focus the variability analysis to quantities of direct interest to the application. Also, there are other aspects of the variability analysis that are not explored in this study; namely, the parameters of the calibration measurements can have a large impact on the transmission model variability; use of different calibration materials and transmission lengths can reduce variability for transmission measurements of interest.

One of the applications of interest for calibration of PCD-based x-ray systems is for quantitative CT. In regards to this application, we point out a couple limitations of the present work. The independent material testing is performed on a single material Teflon slab; and the application to CT would most likely involve subjects composed of two or more tissues. Furthermore, the model testing in this work is performed at the sinogram level, thus it remains to be seen how this model will perform in an actual CT imaging application. Applying the presented model to CT imaging is a topic for future work. In such an application, it is important to understand the implications of the fact that the acquired PCD data need to be processed through the inverse of the NLF functions. The success of this inversion depends on the slope of the NLF function. If the slope is below some threshold value, this inversion is going to be highly unstable and the resulting determination of the incident transmission fraction would be unreliable. These measurements can either be discarded or avoided by reducing the x-ray source flux. Furthermore, the NLF functions may be non-monotonic in which case the correct solution needs to be identified from context.

We have developed a x-ray transmission calibration model for PCDs that allows for the NLF dependence inherent in PCD-based x-ray systems when the x-ray source flux is a significant fraction of the PCD maximum flux rating. The model calibrates the individual energy windows and detector pixels independent of each other and it is accordingly flexible and can be easily adapted to other PCDs. While the results show a good level of accuracy, extensions of the model to include flux-dependent changes in the distributions of the PCD spectral response may reduce the deterministic errors in the transmission model. Such models are more complex than the current proposed model, and if the application of interest can tolerate the current error levels then it is sufficient to exploit the proposed SFR model for PCD calibration in spectral CT imaging.

ACKNOWLEDGMENTS

This work is supported in part by NIH Grant Numbers: R01-EB026282, R01-EB023968, and R21-CA263660. The contents of this paper are solely the responsibility of the authors and do not necessarily represent the official views of the National Institutes of Health.

CONFLICT OF INTEREST

The authors declare that there is no conflict of interest that could be perceived as prejudicing the impartiality of the research reported.

DATA AVAILABILITY STATEMENT

The data for this work are available by contacting the authors.

REFERENCES

1. Yu L, Christner JA, Leng S, Wang J, Fletcher JG, McCollough CH. Virtual monochromatic imaging in dual-source dual-energy CT: Radiation dose and image quality. *Med Phys*. 2011;38:6371-6379.
2. Liu X, Yu L, Primak AN, McCollough CH. Quantitative imaging of element composition and mass fraction using dual-energy CT: Three-material decomposition. *Med Phys*. 2009;36:1602-1609.
3. Wang X, Meier D, Taguchi K, Wagenaar DJ, Patt BE, Frey EC. Material separation in x-ray CT with energy resolved photon-counting detectors. *Med Phys*. 2011;38:1534-1546.
4. Schmidt TG, Sammut BA, Barber RF, Pan X, Sidky EY. Addressing CT metal artifacts using photon-counting detectors and one-step spectral CT image reconstruction. *Med Phys*. 2022;49:3021-3040.
5. Schlomka JP, Roessl E, Dorscheid R, et al. Experimental feasibility of multi-energy photon-counting K-edge imaging in pre-clinical computed tomography. *Phys Med Biol*. 2008;53:4031-4048.
6. Willemink MJ, Persson M, Pourmorteza A, Pelc NJ, Fleischmann D. Photon-counting CT: Technical principles and clinical prospects. *Radiology*. 2018;289:293-312.
7. Schmidt TG. Future prospects of spectral CT: Photon counting. In: Samei E, Pelc NJ, eds. *Computed Tomography Approaches, Applications, and Operations*. Springer; 2020:269-286.
8. Sidky EY, Yu L, Pan X, Zou Y, Vannier M. A robust method of x-ray source spectrum estimation from transmission measurements: Demonstrated on computer simulated, scatter-free transmission data. *J Appl Phys*. 2005;97:124701.
9. Ha W, Sidky EY, Barber RF, Schmidt TG, Pan X. Estimating the spectrum in computed tomography via Kullback–Leibler divergence constrained optimization. *Med Phys*. 2019;46:81-92.
10. Duan X, Wang J, Yu L, Leng S, McCollough CH. CT scanner x-ray spectrum estimation from transmission measurements. *Med Phys*. 2011;38:993-997.
11. Leinweber C, Maier J, Kachelrieß M. X-ray spectrum estimation for accurate attenuation simulation. *Med Phys*. 2017;44:6183-6194.
12. FitzGerald P, Araujo S, Wu M, Man BD. Semiempirical, parameterized spectrum estimation for x-ray computed tomography. *Med Phys*. 2021;48:2199-2213.
13. Taguchi K, Frey EC, Wang X, Iwanczyk JS, Barber WC. An analytical model of the effects of pulse pileup on the energy spectrum recorded by energy resolved photon counting x-ray detectors. *Med Phys*. 2010;37:3957-3969.
14. Danielsson M, Persson M, Sjölin M. Photon-counting x-ray detectors for CT. *Phys Med Biol*. 2021;66:03TR01.
15. Dickmann J, Maier J, Sawall S, et al. A count rate-dependent method for spectral distortion correction in photon-counting CT. *Proc SPIE*. 2018;10573:1057311.
16. Hubbell JH, Seltzer SM. Tables of X-ray mass attenuation coefficients and mass energy-absorption coefficients from 1 keV to 20 MeV for elements $Z = 1$ to 92 and 48 additional substances of dosimetric interest. *Technical Report 5632, NIST, Ionizing Radia-*

tion Division, Physics Laboratory National Institute of Standards and Technology Gaithersburg, MD; 1996.
17. Schmidt TG, Barber RF, Sidky EY. A spectral CT method to directly estimate basis material maps from experimental photon-counting data. *IEEE Trans Med Imag*. 2017:1808-1819.
18. Perkhounkov B, Stec J, Sidky EY, Pan X. X-ray spectrum estimation from transmission measurements by an exponential of a polynomial model. *Proc. SPIE*. 2016;9783:97834W.
19. Cammin J, Xu J, Barber WC, Iwanczyk JS, Hartsough NE, Taguchi K. A cascaded model of spectral distortions due to spectral response effects and pulse pileup effects in a photon-counting x-ray detector for CT. *Med Phys*. 2014;41:041905.
20. Dreier ES, Kehres J, Khalil M, et al. Spectral correction algorithm for multispectral CdTe x-ray detectors. *Opt Engineer*. 2018;57:054117.
21. Nocedal J, Wright S. *Numerical Optimization*. Springer Science & Business Media; 2006.
22. Bujila R, Omar A, Poludniowski G. A validation of SpekPy: A software toolkit for modelling X-ray tube spectra. *Phys Med*. 2020;75:44-54.
23. Touch M, Clark DP, Barber W, Badea CT. A neural network-based method for spectral distortion correction in photon-counting x-ray CT. *Phys Med Biol*. 2016;61:6132-6153.

How to cite this article: Sidky EY, Paul ER, Gilat-Schmidt T, Pan X. Spectral calibration of photon-counting detectors at high photon flux. *Med Phys*. 2022;49:6368–6383. https://doi.org/10.1002/mp.15942

APPENDIX A: JUSTIFICATION OF EQUATION (8)

Consider a single ray originating at the x-ray source and terminating at a given PCD pixel. The emitted intensity along the ray is

$$I_0 = N_0/t, \tag{A.1}$$

where N_0 is the number of photons (fluence) emitted in the measurement time t. The x-ray beam passes through the scanned object, causing attenuation, and, nominally, the beam intensity that is detected at the PCD for energy window w, represents the photon flux for photons that have energies that are in between the threshold settings that define window w. The transmitted intensity at energy window w can be written as

$$I_w^{\text{trans}} = N_w^{\text{trans}}/t, \tag{A.2}$$

where N_w^{trans} is the number of photons in energy window w transmitted through the scanned object. The PCD is susceptible to flux-dependent, nonlinear response effects such as pulse pile-up, and we assume that the flux measurements can be expressed as the following polynomial model:

$$I_w^{\text{meas}} = I_w^{\text{trans}} + \sum_{k=0}^{N} \omega_{w,k} (I_w^{\text{trans}})^k, \tag{A.3}$$

where I_w^{meas} is the model for the measured photon flux in energy window w, and the polynomial is constructed so that $I_w^{\text{meas}} = I_w^{\text{trans}}$ when all coefficients $\omega_{w,k}$ are zero.

Finding the coefficients $\omega_{w,k}$ in Equation (A.3) from experimental measurements of x-ray transmission through an object of known dimensions and composition is not experimentally convenient; access to the true energy-windowed incident flux is needed. In the following, we show that if the measured and transmitted flux can be modeled with Equation (A.3), a similar polynomial model can be used to relate transmitted and measured fractional fluence.

The PCD registers photon fluence, and accordingly, we can manipulate the flux expression so that it relates photon fluences.

$$I_w^{\text{meas}} = N_w^{\text{meas}}/t = (N_w^{\text{trans}}/t) + \sum_{k=0}^{N} \omega_{w,k} (N_w^{\text{trans}}/t)^k. \tag{A.4}$$

Multiplying both sides by t, we obtain

$$N_w^{\text{meas}} = N_w^{\text{trans}} + \sum_{k=0}^{N} \eta_{w,k} (N_w^{\text{trans}})^k, \tag{A.5}$$

where

$$\eta_{w,k} = \omega_{w,k}/t^{k-1}. \tag{A.6}$$

We do not readily have access to N_0 and consequently the number of photons emitted in energy window w, $N_{0,w}$. Thus, it is convenient to relate the model for the measured transmission fluence fraction

$$T_w^{\text{meas}} = N_w^{\text{meas}}/N_{0,w}^{\text{meas}}, \tag{A.7}$$

and the post-object transmission fluence fraction

$$T_w^{\text{trans}} = N_w^{\text{trans}}/N_{0,w}^{\text{trans}}. \tag{A.8}$$

Substituting the transmission fractions into the relation for the measurement model and true transmitted fluence, we obtain

$$T_w^{\text{meas}} \cdot N_{0,w}^{\text{meas}} = T_w^{\text{trans}} \cdot N_{0,w}^{\text{trans}} + \sum_{k=0}^{N} \eta_{w,k} (T_w^{\text{trans}} \cdot N_{0,w}^{\text{trans}})^k. \tag{A.9}$$

Dividing both sides by $N_{0,w}^{\text{meas}}$, the desired model expressed in Equation (8), is obtained

$$T_w^{\text{meas}} = T_w^{\text{trans}} + \sum_{k=0}^{N} \alpha_{w,k} (T_w^{\text{trans}})^k, \tag{A.10}$$

where

$$\alpha_{w,1} = \frac{N_{0,w}^{\text{trans}}}{N_{0,w}^{\text{meas}}}(1 + \eta_{w,1}) - 1, \tag{A.11}$$

and

$$\alpha_{w,k\neq 1} = \frac{(N_{0,w}^{\text{trans}})^k}{N_{0,w}^{\text{meas}}} \eta_{w,k}. \tag{A.12}$$

Relating the α coefficients to the nonlinear intensity model coefficients ω from Equation (A.3), we obtain

$$\alpha_{w,1} = \frac{I_{0,w}^{\text{trans}} t}{I_{0,w}^{\text{meas}} t}(1 + \omega_{w,1}) - 1 = \frac{I_{0,w}^{\text{trans}}}{I_{0,w}^{\text{meas}}}(1 + \omega_{w,1}) - 1, \tag{A.13}$$

and

$$\alpha_{w,k\neq 1} = \frac{(I_{0,w}^{\text{trans}} t)^k}{I_{0,w}^{\text{meas}} t} \frac{\omega_{w,k}}{t^{k-1}} = \frac{(I_{0,w}^{\text{trans}})^k}{I_{0,w}^{\text{meas}}} \omega_{w,k}. \tag{A.14}$$

We note that the α_w coefficients do not depend on the acquisition time t when related to the ω_w coefficients of the nonlinear flux model.

Including the polynomial expression from Equation (A.10) in our calibration model is straightforward because it relates transmitted fluence fractions. If the corresponding nonlinear flux relationship is desired then the ω coefficients can be solved for using Equations (A.13) and (A.14), but doing so requires access to $I_{0,w}^{\text{trans}}$ and an estimate of $I_{0,w}^{\text{meas}}$. We also note that pulse pile-up is a flux-dependent phenomenon, thus the ω coefficients are independent of the measurement time. Interestingly in relating the α coefficients to the ω coefficients we observe that the acquisition time cancels out; thus, different acquisition times can be used for calibration and spectral CT projection measurements. The fitted α coefficients for the model in Equation (A.10) will still be valid.